

# MPDR Beamforming for Almost-Cyclostationary Processes

Giovanni Bologni, Martin Bo Møller, Richard Heusdens and Richard C. Hendriks

**Abstract**—Conventional acoustic beamformers typically assume short-time stationarity and process frequency bins independently, ignoring inter-frequency correlations. This is suboptimal for almost-periodic noise sources such as engines, fans, and musical instruments: these signals are better modeled as (almost) cyclostationary (ACS) processes with statistically correlated spectral components. This paper introduces the cyclic minimum power distortionless response (cMPDR) beamformer, which extends the conventional MPDR to jointly exploit spatial and spectral correlations. Building on frequency-shifted (FRESH) filtering, it suppresses noise components that are coherent across harmonically related frequencies, reducing residual noise beyond what spatial filtering alone achieves. To address inharmonicity, where partials deviate from exact integer multiples of a fundamental frequency, we estimate resonant frequencies from a periodogram and derive frequency shifts from their pairwise spacing. Theoretical analysis yields closed-form expressions for residual noise and proves that output power decreases monotonically with the number of cyclic components. Experiments on synthetic harmonic noise and real UAV motor recordings confirm these findings: in low-SNR scenarios, the cMPDR achieves up to 5 dB improvement in SI-SDR over the MPDR, yields consistent STOI gains, and remains effective with a single microphone. When spectral correlation is absent, the method reduces to conventional MPDR and does not degrade performance. These results suggest that cyclic processing is a viable direction for acoustic noise reduction that deserves further investigation. Code is available at <https://github.com/Screen/cMPDR>.

**Index Terms**—Beamforming, almost-cyclostationary, FRESH.

## I. INTRODUCTION

RECOVERING a weak target signal in acoustic environments dominated by structured, periodic noise remains a challenge in acoustic signal processing and for industrial communication systems [1]. Conventional single- and multi-channel speech enhancement methods, including approaches based on deep neural networks (DNNs) [2], [3], [4], [5] and classical power spectral density (PSD) techniques such as spectral subtraction or Wiener filtering, often struggle in extreme low signal-to-noise ratio (SNR) regimes where the target is entirely masked by high-energy interference [6], [7]. Additionally, DNNs cannot easily be constrained to preserve a signal from a target direction [8], and they can be sensitive to training data.

Spatial filtering, exemplified by the minimum power distortionless response (MPDR) beamformer, offers a partial

This work was partly supported by the Dutch Research Council (NWO) and partly by the Signal Processing Systems Group, Delft University of Technology, Delft, The Netherlands. Giovanni Bologni, Richard Heusdens, and Richard C. Hendriks are with the Faculty of Electrical Engineering, Mathematics, and Computer Science, Delft University of Technology, The Netherlands (e-mails: G.Bologni@tudelft.nl; R.Heusdens@tudelft.nl; R.C.Hendriks@tudelft.nl). Richard Heusdens is also with Netherlands Defence Academy, 1781 AC Den Helder, The Netherlands. Martin Bo Møller is with Bang & Olufsen, Struer, 7600, Denmark (e-mail: acoustics.moeller@gmail.com), Corresponding author: Giovanni Bologni.

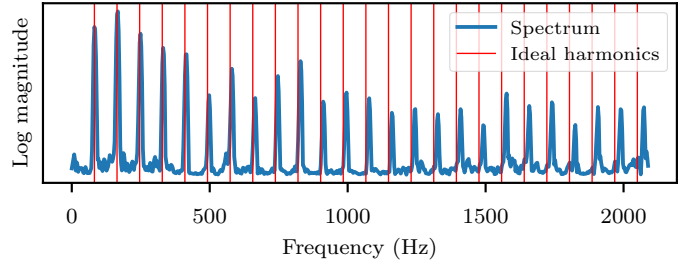


Fig. 1: Spectrum of a cello note (E2  $\approx$  82 Hz) with ideal harmonics. Higher harmonics deviate from integer multiples of the fundamental.

solution [9], [10]. The MPDR minimizes received power while preserving the signal from a target direction [11], [12]. Standard implementations in the short-time Fourier transform (STFT) domain assume the signal is wide-sense stationary (WSS), implying that different frequency bins are uncorrelated [13].

However, acoustic noise from rotating machinery, drones, and ventilation fans, exhibits periodic fluctuations better described by the cyclostationary (or periodically correlated) model [14], [15], [16], [17], [18]. The key distinction between cyclostationary (CS) and WSS processes lies in their frequency-domain behavior: CS signals possess statistical dependencies between harmonically related frequency bins. Frequency-shift (FRESH) filters can exploit these spectral correlations to separate CS signals that overlap in both time and frequency, provided they possess distinct cyclic frequencies [19]. These filters have long been used in telecommunications to localize and extract target CS signals from noise [20], [21], [22], [23], [24], [25]. More recently, the application of FRESH beamforming to mechanical fault localization has also been explored [26]. However, most FRESH-based approaches are developed for telecommunications and assume strict cyclostationarity, where cyclic frequencies are known exactly and reside on a uniform harmonic grid. Such rigid models are ill-suited for physical acoustic sources, which are more accurately characterized as almost-cyclostationary (ACS).

In ACS processes, inharmonicity causes spectral correlations to deviate from the ideal harmonic series. Physical mechanisms drive this inharmonicity: in string instruments, finite stiffness causes higher partials to drift sharp [27]; Fig. 1 illustrates this effect using a recording of a cello playing the note E2 [28]. In vibrating objects with multiple spatial degrees of freedom, such as drumheads, spectral components may occur at non-harmonic frequencies altogether. Conventional cyclic methods that rely on fixed harmonic structures fail when these deviations occur, as the expected correlation between bins vanishes [29], [30], Fig. 1d]. This mismatch between CS model and ACS reality prevents traditional FRESH filters from effectively exploiting the spectral redundancy of the signal.

In the acoustic domain, cyclostationarity has primarily been

arXiv:2510.18391v2 [eess.AS] 19 Mar 2026

leveraged to model the target speech. In the context of speech enhancement, Jensen *et al.*, [31] focused on modeling speech as a harmonic signal with energy concentrated at integer multiples of a fundamental, while still assuming spectral uncorrelation. Following this, a cyclic multichannel Wiener filter (cMWF) that exploits the CS property of voiced speech was proposed [30]. However, these approaches face two limitations. First, tracking the rapidly varying fundamental frequency and spectral statistics of speech is difficult. Second, they rely on the strict harmonic model, where cyclic frequencies are exact integer multiples of a fundamental, which clashes with the inharmonic reality of acoustic sources described above. We therefore shift our attention from the highly varying target to the more stable, dominant interferer. By exploiting the spectral redundancy of the ACS noise rather than the target, distortionless recovery becomes possible even when the target lacks periodic structure or is too variable to track reliably. Table I positions the cMPDR against prior cyclostationary methods.

In this paper, we propose the cyclic minimum power distortionless response (cMPDR) beamformer, a model-based algorithm for cancelling dominant ACS interferers. By augmenting the observation vector with frequency-shifted versions of the input, the cMPDR exploits the statistical redundancy of the interferer to steer nulls in both space and frequency, while providing distortionless guarantees for the target signal. This allows for the recovery of weak signals even in single-channel configurations where spatial discrimination is impossible. To handle the challenges of inharmonicity and partial correlation inherent to ACS signals, we introduce two technical innovations. First, a *difference-based shift calculation* strategy estimates individual harmonic components via periodogram analysis and computes frequency shifts based on measured differences, rather than assuming a perfect harmonic series. This data-driven approach allows the cMPDR to adapt to the true spectral support of the noise. Second, a *coherence-based shift selection* mechanism identifies which spectral dependencies are strong enough to exploit, pruning weakly correlated components. The coherence filtering also ensures graceful degradation to the classical MPDR when cyclostationary structure is absent, making the method robust to model mismatch.

Theoretical analysis yields closed-form expressions for the residual noise power and output SNR as a function of spectral correlation, and proves that adding cyclic components does not degrade performance. Experiments on synthetic harmonic noise, real UAV motor recordings (DREGON dataset), and non-stationary noise (Freesound/MUSAN dataset) confirm these predictions, with scale-invariant signal-to-distortion-ratio (SI-SDR) gains of up to 5 dB over MPDR in low-SNR conditions and consistent intelligibility improvements. Under non-stationary noise without persistent spectral correlation, cMPDR reduces to MPDR, exhibiting identical performance.

Our contributions are as follows. (i) We introduce the cMPDR, a generalized interference cancellation framework that exploits spectral and spatial correlations of the dominant noise rather than the target signal. This approach enables distortionless recovery of weak signals even when the target is buried beneath the noise floor (*e.g.* SNR  $\leq -10$  dB). (ii) We provide a theoretical analysis quantifying the subband

SNR gains achievable by exploiting spectral redundancy. We demonstrate that the noise reduction capability is directly proportional to the spectral correlation of the interference, providing a predictable measure of the performance advantage over conventional spatial-only beamforming. (iii) We present a difference-based shift calculation to handle the inharmonicity inherent in acoustic sources. Rather than assuming cyclic frequencies at exact integer multiples of a fundamental, this method identifies spectral dependencies regardless of their harmonic spacing. (iv) We integrate a coherence filtering mechanism to address the partial correlation of harmonics typical of ACS signals. This mechanism prunes frequency shifted components that are weakly correlated with the original bin, preventing artefacts that occur when the harmonic coupling is weak.

## II. BACKGROUND

### A. Cyclostationary processes

This section introduces the definition of CS processes and their spectral representation. Time-domain random processes are denoted by a bar. A real-valued discrete-time random process  $\{\bar{x}(n), n \in \mathbb{Z}\}$  is wide-sense *cyclostationary* if both its mean and covariance function are periodic with some period  $P$ :

$$m_{\bar{x}}(n) = m_{\bar{x}}(n + P), \quad (1)$$

$$r_{\bar{x}}(n, \tau) = r_{\bar{x}}(n + P, \tau), \quad \forall n, \tau \in \mathbb{Z}. \quad (2)$$

In other words, the statistical properties of the process repeat every  $P$  samples. As the mean and the covariance of a CS process are periodic in  $n$  with period  $P$ , they accept a Fourier series expansion over a set of *cyclic frequencies*

$$\mathcal{A}_{CS} = \{\alpha_p = 2\pi p/P\}_{p=0}^{P-1}. \quad (3)$$

These are the frequencies at which the statistics oscillate. A cyclic frequency  $\alpha_p$  is also referred to as a *resonant frequency* of the process. By expanding  $r_{\bar{x}}(n, \tau)$  in a Fourier series with respect to  $n$  and applying a discrete-time Fourier transform with respect to  $\tau$ , we get a function  $S_x(\alpha_p, \omega)$  of two frequency variables: the *cyclic* frequency  $\alpha_p$  and the *spectral* frequency  $\omega$  (assuming convergence of the infinite sum):

$$S_x(\alpha_p, \omega) = \sum_{\tau=-\infty}^{\infty} \sum_{n=0}^{P-1} r_{\bar{x}}(n, \tau) e^{-j(\alpha_p n + \omega \tau)}. \quad (4)$$

This quantity is known as spectral correlation density (SCD), or cyclic spectrum, as for finite-length processes<sup>1</sup> it is also given by [15]:

$$S_x(\alpha_p, \omega_k) = \mathbb{E}[x(\omega_k) x^*(\omega_k - \alpha_p)], \quad (5)$$

<sup>1</sup>A random process with support other than  $(-\infty, \infty)$  cannot be CS. Yet, if the process is CS within a much longer time interval than the interval relevant for the application, the process may be regarded as *effectively CS*, and the standard machinery of CS processes can be applied [33].

TABLE I: Comparison of representative cyclostationary-based methods. Most prior work was developed for telecommunications or mechanical signal analysis, whereas only limited work exists in audio signal processing. \*: this work is about localization.

Method	Application domain	Cyclostationarity exploited in	Supports unknown cyclic frequencies	Rejects weakly correlated cyclic components	Multi-channel	Distortion-less
FRESH [19]	Comm.	Target+noise	No	No	No	No
Cyclic MUSIC* [20]	Comm.	Target	Yes	No	No	No
Cyclo BF* [26]	Mech.	Target	No	No	Yes	No
BA-FRESH [32]	Comm.	Target	No	No	No	No
FRESH BF [24], [25]	Comm.	Target	No	No	Yes	No
FRESH-LCMV [21], [22]	Comm.	Target	No	No	Yes	Yes
Adaptive-FRESH [29]	Comm.	Target	No	No	No	No
cMWF [30]	Audio	Target	No	No	Yes	No
<b>cMPDR (proposed)</b>	<b>Audio</b>	<b>Noise</b>	<b>Yes</b>	<b>Yes</b>	<b>Yes</b>	<b>Yes</b>

where  $x(\omega_k)$  denotes the process given by the  $K$ -point Fourier transform of  $\{\bar{x}_{[K]}(n), n = 0, \dots, K-1\}$ ,

$$x(\omega_k) = \sum_{n=0}^{K-1} \bar{x}_{[K]}(n) e^{-j\omega_k n}. \quad (6)$$

The SCD in Eq. (5) measures the correlation between the frequency component at  $\omega_k$  and the component at  $\omega_k - \alpha_p$ , that is separated by the cyclic frequency  $\alpha_p$ . The SCD boils down to the conventional power spectral density (PSD)  $S_x(\omega_k)$  for  $\alpha_p = 0$ :

$$S_x(0, \omega_k) = S_x(\omega_k) = \mathbb{E}[|x(\omega_k)|^2]. \quad (7)$$

In other words, when  $\alpha_p = 0$ , we recover the standard PSD, which measures power at each frequency without considering correlations between different frequencies. We also introduce a normalized version of the cyclic spectrum, called spectral coherence, which is given by [34], [35]:

$$\gamma_x(\alpha_p, \omega_k) = \frac{|S_x(\alpha_p, \omega_k)|^2}{S_x(\omega_k) S_x(\omega_k - \alpha_p)}, \quad (8)$$

where  $0 \leq \gamma_x(\alpha_p, \omega_k) \leq 1$ . The normalization makes the spectral coherence easier to interpret: values close to 1 indicate strong correlation between the frequency components. A key property of CS processes is to exhibit inter-frequency correlations that can be measured by the cyclic spectrum or the spectral coherence. In fact,  $x(\omega_1)$  is correlated with  $x(\omega_2)$  for  $|\omega_1 - \omega_2| = \alpha_p$ , for every  $\alpha_p \in \mathcal{A}_{CS}$ . Intuitively, if we measure  $x(\omega_1)$ , we know something about  $x(\omega_2)$ . In contrast, the spectral components of WSS processes are asymptotically uncorrelated. For example, for white Gaussian noise, we have that  $S_x(\alpha_p, \omega_k) = \gamma_x(\alpha_p, \omega_k) = 0$  for all  $\alpha_p \neq 0$ . This means that for WSS processes, knowing the power at one frequency does not tell us anything about the power at another frequency. Notice that all quantities in this section are defined for a single random process, but generalizing the notions to the cross-statistics between multiple processes is straightforward.

Real-world acoustic signals are often not strictly periodic and are therefore more appropriately modeled as ACS processes [36]. In contrast to strictly CS models, the cyclic frequencies are not restricted to integer multiples of a single fundamental but may take arbitrary values, leading to non-uniform spectral

spacing. We define the cyclic set

$$\mathcal{A}_{ACS} = \mathcal{A} = \{\alpha_p\}_{p=0}^{P-1} \quad (9)$$

which contains all cyclic frequencies at which second-order spectral correlations occur. In the acoustic scenarios discussed in the introduction,  $\mathcal{A}$  is generally inharmonic and unknown, and will be estimated from data in Section V-A. For a detailed treatment of the theory of ACS processes, see [17, Sec. 3.2].

### B. Estimation of the cyclic spectrum

The cyclic spectrum, defined in Eq. (5), is given by the ensemble expectation of the product of the signal at frequencies  $\omega_k$  and  $\omega_k - \alpha_p$ . In the beamforming context considered here, the SCD is estimated by a finite temporal average over data. Next, since  $\omega_k$  is by definition a DFT sampling point but  $\omega_k - \alpha_p$  generally is not, the frequency shift must be handled explicitly. One could approximate it by increasing the DFT size to obtain a finer resolution, but this would be computationally inefficient. A more practical approach is to modulate the signal in the time domain by  $e^{j\alpha_p n}$ , which shifts the spectrum prior to applying a standard DFT. The resulting *time-averaged cyclic periodogram* (ACP) provides a widely used estimator of the cyclic spectrum [37]. The ACP coincides with the Welch PSD estimator for  $\alpha_p = 0$  [38], and under mild regularity conditions it yields consistent SCD estimates even from a single record [37]. Other methods for SCD estimation may offer faster computations if knowledge of the cyclic spectrum at all spectral and cyclic frequencies is required [39], [40], [41]. However, since we require the SCD only for a limited set of cyclic frequencies, the ACP is well suited to our needs.

To implement the ACP, we first modulate the signals in the time-domain, then process them in the STFT domain. Let  $\{\bar{x}(n), n \in \mathbb{Z}\}$  and  $\{\bar{y}(n), n \in \mathbb{Z}\}$  be random processes sampled with sampling frequency  $f_s$ , and define  $\{\bar{x}_{[N]}(n)\}$  and  $\{\bar{y}_{[N]}(n)\}$  to equal  $\{\bar{x}(n)\}$  and  $\{\bar{y}(n)\}$  for  $n = 0, \dots, N-1$  and zero elsewhere. Using a discrete Fourier transform (DFT) with size  $K$  and hop size  $R$ , we obtain  $L = \lceil 1 + (N-K)/R \rceil$  STFT frames, where  $\lceil \cdot \rceil$  is the ceiling function. The DFT length determines the spectral resolution  $\Delta\omega \approx f_s/K$  [Hz]. By contrast, the spacing between resolvable cyclic frequencies follows from the total number  $LR$  of observed samples,  $\Delta\alpha \approx f_s/(LR)$  [Hz], even though we only evaluate the SCD for a small number of cyclic shifts [37]. As mentioned earlier,

these cyclic shifts do not generally align with the DFT bin spacing of  $1/K$ . Rather than extracting  $x(\omega_k - \alpha_p)$  by shifting the spectrum, we achieve the shift by modulating the time-domain signal with  $e^{j\alpha_p n}$  before taking the DFT, exploiting the modulation property:

$$x(\omega_k - \alpha_p) \xleftrightarrow{\mathcal{F}} \bar{x}_{[N]}(n)e^{j\alpha_p n}. \quad (10)$$

The modulated signal in the time domain and its STFT counterpart are given by:

$$\bar{x}_{[N]}^{(\alpha_p)}(n) = \bar{x}_{[N]}(n)e^{jn\alpha_p}, \quad (11)$$

$$x(\omega_k - \alpha_p, \ell) = \sum_{n=0}^{K-1} \bar{x}_{[N]}^{(\alpha_p)}(n + \ell R)w(n)e^{-jn\omega_k}, \quad (12)$$

where  $\ell$  is the time-frame index and  $w(n)$  is a window function with support in  $\{0, \dots, K-1\}$ . The ACP estimate at cyclic frequency  $\alpha_p$  and spectral frequency  $\omega_k$  is then given by:

$$\hat{S}_{yx}(\alpha_p, \omega_k) = \frac{1}{L} \sum_{\ell=0}^{L-1} y(\omega_k, \ell)x^*(\omega_k - \alpha_p, \ell). \quad (13)$$

Likewise, the spectral coherence can be estimated as:

$$\hat{\gamma}_{yx}(\alpha_p, \omega_k) = \frac{|\hat{S}_{yx}(\alpha_p, \omega_k)|^2}{\hat{S}_y(\omega_k)\hat{S}_x(\omega_k - \alpha_p)}, \quad (14)$$

where the regularized PSDs are defined as

$$\hat{S}_y(\omega_k) = \max\{\hat{S}_y(\omega_k), \hat{S}_y^{\max}/D_{\text{PSD}}\}, \quad \hat{S}_y^{\max} = \max_{\omega_k} \hat{S}_y(\omega_k),$$

and similarly for  $\hat{S}_x(\omega_k - \alpha_p)$ . By constraining the PSDs to be at least  $1/D_{\text{PSD}}$  of their peak value, this approach avoids divisions by near-zero values.

### C. Relation to cross-band filter and frequency leakage models

The spectral correlations defined in Section II-A arise from the source itself: the periodicity of an ACS process induces statistical dependencies between harmonically related bins, as captured by the SCD in Eq. (5). Two other mechanisms produce cross-band correlations that are unrelated to source periodicity and should not be confused with the above. First, convolution with a long room impulse response introduces cross-band coupling, modeled by cross-band filters and exploited through the convolutive transfer function (CTF) model [42], [43], [44]; this is a property of the acoustic system. Second, STFT windowing causes frequency leakage, inducing spurious correlations between adjacent bins [45], [46]; this is an artifact of the processing chain. Both effects are largely confined to bins in the immediate vicinity of the working frequency, whereas ACS links distant harmonic components across the full spectrum; the three families of methods are thus complementary rather than contradictory.

### D. Single-band beamforming

Following the overview of cyclostationary theory and methods, we now examine classical beamforming theory. We denote matrices by bold capitals and vectors by bold lowercase letters. Let  $\mathbf{x}(\omega_k, \ell) = [x_0(\omega_k, \ell) \dots x_{M-1}(\omega_k, \ell)]^T \in \mathbb{C}^M$

represent noisy and reverberant measurements from a  $M$ -elements microphone array in the STFT domain at time-frame  $\ell$ . Hereafter, the time-frame index  $\ell$  is omitted for simplicity. The measurements are modeled as:

$$\mathbf{x}(\omega_k) = s(\omega_k)\mathbf{a}(\omega_k) + \mathbf{v}(\omega_k) = \mathbf{d}(\omega_k) + \mathbf{v}(\omega_k), \quad (15)$$

where  $\mathbf{a}(\omega_k) = [1 \ a_1(\omega_k) \dots a_{M-1}(\omega_k)]^T$  is the relative transfer function (RTF) between a reference sensor and the remaining sensors,  $s(\omega_k)$  denotes the target signal at the reference microphone, and  $\mathbf{v}(\omega_k)$  represents additive noise. Without loss of generality, the first sensor is chosen as the reference. The time-domain convolution of the signal and room impulse response (RIR) is approximated by a multiplication in the STFT domain, assuming the reverberation time is much shorter than a single STFT frame [47]. The general goal of beamforming is to estimate a target signal as a linear combination of the noisy inputs. A popular approach is the MPDR beamformer, which is formulated as the solution to:

$$\begin{aligned} \min_{\mathbf{w}(\omega_k)} \quad & \mathbb{E}[|\mathbf{w}^H(\omega_k)\mathbf{x}(\omega_k)|^2] \\ \text{s.t.} \quad & \mathbf{w}^H(\omega_k)\mathbf{a}(\omega_k) = 1, \end{aligned} \quad (16)$$

where the goal is to reduce the power of the noisy signal as much as possible while retaining signals whose transfer function is  $\mathbf{a}(\omega_k)$ .

## III. PROPOSED CMPDR BEAMFORMER

This section presents the proposed cMPDR beamformer. The design extends the single-band model in Eq. (15) to a multi-band model, in which the received signal is evaluated at multiple, arbitrary frequencies, and the corresponding signal components are highly correlated. In the following, we refer to these as ‘‘frequency-shifted’’ components, since evaluation at arbitrary frequencies is carried out by modulating the time-domain signal prior to the STFT (see Section II-B).

Before introducing the multi-band model, consider the example in Fig. 2 to build intuition on FRESH beamforming. The same cello recording as in Fig. 1 ( $f_1 \approx 82$  Hz) is used, as musical instrument recordings exhibit high spectral coherence. The signal is decomposed into its first three harmonics by bandpass filtering around  $n \cdot f_1$  for  $n = 1, 2, 3$ . Each harmonic is then frequency-shifted (down-modulated) to  $f_1$  and passed through a second bandpass filter centered at  $f_1$ . The three rows in Fig. 2 correspond to these processed harmonics ( $n = 1, 2, 3$ ), i.e., the signals obtained after downshifting each harmonic to the same frequency. This sequence mirrors the processing steps before beamforming (see Fig. 4), and the resulting signals are shown in the time domain for visualization. For the cello signal (Fig. 2a), the three downshifted components appear nearly identical up to a scaling and delay, indicating that they can be linearly combined. This property is known as *spectral redundancy* [48]. By contrast, applying the same steps to white noise (Fig. 2b) yields components that exhibit no visible similarity and behave as independent realizations.

### A. Modulation sets $\mathcal{M}_k$

For each frequency bin  $k$ , the multi-band signal is formed by concatenating the received signal with its frequency-shifted

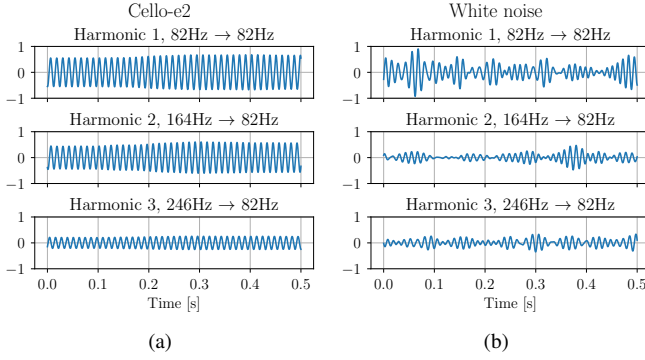


Fig. 2: Waveforms of cello (a) and white noise (b) after bandpass filtering around the first three harmonics and downshifting each component to 82 Hz, the fundamental frequency of the note. Each row corresponds to one frequency-shifted harmonic ( $n = 1, 2, 3$ ), forming the inputs to the cMPDR beamformer. The cello components are highly correlated, while the white noise components appear uncorrelated.

versions. The applied shifts are collected in the *modulation set*

$$\mathcal{M}_k = \{\mu_{c_k}\}_{c_k=0}^{C_k-1}, \quad k = 0, \dots, K-1, \quad (17)$$

where  $C_k$  is the cardinality of the set, and  $\mu_{c_k}$  is a linear combination of the cyclic frequencies. By convention, the first element is  $\mu_{0_k} = 0$ , corresponding to no modulation. Depending on how the elements of  $\mathcal{M}_k$  are chosen, the multi-band model accommodates spectral correlations in either the target or the noise signal. In this work, the shifts are selected based on the resonant frequencies of the noise, so the noise is modeled as ACS while the target is assumed WSS, or possibly ACS with distinct cyclic frequencies. In what follows,  $\mathcal{M}_k$  is assumed known; estimation is addressed in Section V.

### B. Multi-band signal model

In the multi-band model, the received signal and its shifted counterparts are stacked into the vector  $\mathbf{x}(\mathcal{M}_k, \omega_k) \in \mathbb{C}^{MC_k}$ , where  $M$  is the number of microphones:

$$\mathbf{x}(\mathcal{M}_k, \omega_k) = \begin{bmatrix} \mathbf{x}(\omega_k) & \mathbf{x}(\omega_k - \mu_{1_k}) & \cdots & \mathbf{x}(\omega_k - \mu_{C_k-1}) \end{bmatrix}^T, \quad (18)$$

For  $M = 1$ , each element of this vector corresponds to one of the rows in Fig. 2a (shown in the time domain for visualization): the first element is the signal at  $\omega_k$  (row 1), the second is the signal shifted by  $\mu_{1_k}$  (row 2), and so on. The modulated noise vector  $\mathbf{v}$  and reverberant signal vector  $\mathbf{d}$  are constructed similarly:

$$\mathbf{v}(\mathcal{M}_k, \omega_k) = \begin{bmatrix} \mathbf{v}(\omega_k) & \mathbf{v}(\omega_k - \mu_{1_k}) & \cdots & \mathbf{v}(\omega_k - \mu_{C_k-1}) \end{bmatrix}^T. \quad (19)$$

To simplify notation, we omit explicit dependencies on  $\mathcal{M}_k$  and  $\omega_k$  from this point onward. The modulated reverberant signal  $\mathbf{d}$  can be expressed as  $\mathbf{d} = \mathbf{A}\mathbf{s}$ , where  $\mathbf{s} = [s(\omega_k) \dots s(\omega_k - \mu_{C_k-1})]^T \in \mathbb{C}^{C_k}$  is the modulated signal at the reference microphone, and  $\mathbf{A} \in \mathbb{C}^{MC_k \times C_k}$  contains zero-padded, frequency-shifted RTFs. As an example, for the

special case  $C_k = 2$ ,  $\mathbf{d}$  is given by:

$$\mathbf{d} = \mathbf{A}\mathbf{s} = \begin{bmatrix} \mathbf{a}(\omega_k) & \mathbf{0}_{M(C_k-1)} \\ \mathbf{0}_{M(C_k-1)} & \mathbf{a}(\omega_k - \mu_{1_k}) \end{bmatrix} \begin{bmatrix} s(\omega_k) \\ s(\omega_k - \mu_{1_k}) \end{bmatrix}, \quad (20)$$

where  $\mathbf{0}_N$  represents a zero vector of size  $N$ . The resulting multi-band signal model can now be expressed as:

$$\mathbf{x} = \mathbf{d} + \mathbf{v} \in \mathbb{C}^{MC_k}. \quad (21)$$

Let us also define

$$\mathbf{S}_{\mathbf{x}}(\mathcal{M}_k, \omega_k) = \mathbf{S}_{\mathbf{x}} = \mathbb{E}[\mathbf{x}\mathbf{x}^H] \in \mathbb{C}^{MC_k \times MC_k} \quad (22)$$

as the spectral-spatial covariance matrix across microphones and cyclic frequencies, where each entry corresponds to a cyclic spectrum. In practice, the elements of  $\mathbf{S}_{\mathbf{x}}$  are estimated using the ACP method detailed in Section II-B per spectral frequency  $\omega_k$ , cyclic frequency  $\mu_{c_k} \in \mathcal{M}_k$  and microphone pair. Notice that, for  $\mathcal{M}_k = \{0\}$ , we have that

$$\mathbf{S}_{\mathbf{x}}(\{0\}, \omega_k) = \mathbf{S}_{\mathbf{x}}(\omega_k) \in \mathbb{C}^{M \times M}, \quad (23)$$

i.e., the spectral-spatial covariance matrix reduces to the spatial covariance matrix if only the null modulation is considered. We additionally assume that the complex signals under analysis are *proper*, meaning that their conjugate covariance vanishes,  $\mathbb{E}[\mathbf{x}\mathbf{x}^T] = \mathbf{0}$ , and can thus be ignored hereafter [49], [50].

### C. Beamformer design

Based on the multi-band signal model, we design a beamformer that jointly processes microphones and frequency-shifted components. Exploiting the spectral correlations captured in  $\mathbf{S}_{\mathbf{x}}$ , the beamformer minimizes the total output power across cyclic frequencies while enforcing a distortionless constraint for the desired RTF, analogous to the single-band MPDR. The resulting cMPDR is obtained as the solution of the following optimization problem:

$$\begin{aligned} \min_{\mathbf{w}} \quad & \mathbb{E}[|\mathbf{w}^H \mathbf{x}|^2] \\ \text{s.t.} \quad & \mathbf{w}^H \mathbf{a}_0 = 1, \end{aligned} \quad (24)$$

where  $\mathbf{a}_0 = [\mathbf{a}^T(\omega_k) \mathbf{0}_{M(C_k-1)}^T]^T = \mathbf{A}\mathbf{e}_1$  is the target RTF padded with zeroes, corresponding to the first column of  $\mathbf{A}$ , and  $\mathbf{e}_1$  is the standard basis vector of size  $C_k$ , with 1 at the first position and 0 elsewhere. The solution to this problem is given by

$$\mathbf{w}_{\text{cMPDR}} = \frac{\mathbf{S}_{\mathbf{x}}^{-1} \mathbf{a}_0}{\mathbf{a}_0^H \mathbf{S}_{\mathbf{x}}^{-1} \mathbf{a}_0}. \quad (25)$$

To improve the conditioning of the estimated covariance matrix we employ diagonal loading (see Section VI for details). The multi-band noisy input  $\mathbf{x}$  contains the desired component  $\mathbf{d}(\omega_k)$ , its modulated counterparts  $\mathbf{d}(\omega_k - \mu_{c_k})$ ,  $c_k = 1, \dots, C_k - 1$ , and the corresponding noise terms.

The constraint  $\mathbf{w}^H \mathbf{a}_0 = 1$  preserves only the non-modulated target at the reference microphone,  $d_0(\omega_k)$ . The modulated target components are not explicitly constrained. Introducing additional constraints, as in a linearly constrained minimum variance (LCMV) formulation, would require knowledge of the corresponding RTFs and reduce the achievable noise

suppression [21]. Instead, by minimizing the total output power  $\mathbb{E}[\mathbf{w}^H \mathbf{x}]^2$ , the proposed design treats the modulated target components as interference and suppresses them implicitly. In the conventional single-band formulation, minimizing total output power (MPDR) and minimizing noise power, i.e., the minimum variance distortionless response (MVDR) criterion, lead to the same solution. In the present multi-band formulation, this equivalence no longer holds: a cyclic MVDR, obtained by minimizing noise power only, would not penalize the modulated target components and would leave them at the output, whereas the proposed cMPDR suppresses them by minimizing total output power.

#### IV. STATISTICAL ANALYSIS OF THE cMPDR

This section analyzes three statistical properties of the cMPDR beamformer. For clarity, we focus on a single frequency bin  $\omega_k$  and set  $C_k = 2$  resulting in  $\mathcal{M}_k = \{0, \mu_{1k}\}$ . This simplified setting provides insight into the behavior of the cyclic beamformer. First, we show that when the received signal is spectrally uncorrelated, the cMPDR reduces exactly to the classical MPDR. Next, we compute the residual noise power and corresponding SNR improvements in closed form for  $M = 1$ . Finally, we show that in the general case the residual noise power decreases monotonically with  $C_k$  when spectral correlation is present.

##### A. Spectrally uncorrelated components

Consider a spectral component that is uncorrelated with its frequency-shifted counterpart. If  $\mathbf{x}(\omega_k)$  is spectrally uncorrelated with  $\mathbf{x}(\omega_k - \mu_{1k})$ , then  $\mathbb{E}[\mathbf{x}(\omega_k)\mathbf{x}(\omega_k - \mu_{1k})^H] = \mathbf{0}$ , and the covariance matrix  $\mathbf{S}_x$  becomes block-diagonal. The numerator of Eq. (25) simplifies to

$$\mathbf{S}_x^{-1} \mathbf{a}_0 = \begin{bmatrix} \mathbf{S}_x^{-1}(0, \omega_k) & \mathbf{0} \\ \mathbf{0} & \mathbf{S}_x^{-1}(\mu_{1k}, \omega_k) \end{bmatrix} \begin{bmatrix} \mathbf{a}(\omega_k) \\ \mathbf{0} \end{bmatrix}, \quad (26)$$

where we used the fact that the inverse of a block-diagonal matrix is a block-diagonal matrix whose blocks are the inverses of the original blocks. Substituting Eq. (23) into Eq. (26), and Eq. (26) into Eq. (25), it follows that the cMPDR reduces to the MPDR:  $\mathbf{w}_{\text{cMPDR}} = [\mathbf{w}_{\text{MPDR}}^T \mathbf{0}^T]^T$ . This implies that cyclic beamforming provides benefit only at frequencies where the noise exhibits spectral correlation, which typically occurs at the harmonic components. Including additional frequency-shifted components  $\mathbf{x}(\omega_k - \mu_{2k}), \mathbf{x}(\omega_k - \mu_{3k}), \dots$  does not change the conclusion, provided that all such components are mutually uncorrelated and uncorrelated with  $\mathbf{x}(\omega_k)$ .

##### B. Noise reduction performance: effects of correlation

To isolate the effect of spectral correlation on the noise reduction performance, we restrict our analysis to the single-microphone case ( $M = 1$ ). We follow a similar procedure as in [50]. In this setting, the noisy signal is given by:

$$\mathbf{x} = \begin{bmatrix} s(\omega_k) \\ s(\omega_k - \mu_{1k}) \end{bmatrix} + \begin{bmatrix} v(\omega_k) \\ v(\omega_k - \mu_{1k}) \end{bmatrix}. \quad (27)$$

Assuming that the target and noise are uncorrelated and that  $s(\omega_k)$  and  $s(\omega_k - \mu_{1k})$  are uncorrelated, the noisy spectral covariance matrix is given by:

$$\mathbf{S}_x = \underbrace{\begin{bmatrix} \sigma_s^2 & 0 \\ 0 & 0 \end{bmatrix}}_{\mathbf{S}_s} + \underbrace{\begin{bmatrix} 0 & 0 \\ 0 & \sigma_m^2 \end{bmatrix}}_{\mathbf{S}_m} + \underbrace{\sigma_v^2 \begin{bmatrix} 1 & \rho \\ \rho & 1 \end{bmatrix}}_{\mathbf{S}_v} \quad (28)$$

where  $\sigma_s^2 = \mathbb{E}[|s(\omega_k)|^2]$  is the PSD of the target,  $\sigma_m^2 = \mathbb{E}[|s(\omega_k - \mu_{1k})|^2]$  is the PSD of the modulated target component, which arises as a processing artefact and should *not* be present at the output of the beamformer,  $\sigma_v^2$  is the noise PSD, and  $-1 \leq \rho \leq 1$  denotes the spectral correlation of the noise, where  $\rho = 0$  denotes spectrally uncorrelated, therefore stationary noise, and  $|\rho| = 1$  denotes perfectly correlated (harmonic) noise. The overall noise covariance is  $\mathbf{S}_n = \mathbf{S}_m + \mathbf{S}_v$  and should be as small as possible after filtering. The cMPDR minimizes  $\mathbf{w}^H \mathbf{S}_x \mathbf{w}$  subject to preserving the non-modulated target component  $s(\omega_k)$ . In this example, the distortionless response constraint reduces to

$$\mathbf{a}_0^H \mathbf{w}_c = [1 \ 0] \mathbf{w}_c = 1 \iff \mathbf{w}_c = [1 \ y]^T, \quad (29)$$

as  $\mathbf{a}_0$  is normalized being an RTF. The optimal cMPDR beamformer is then in the form  $\mathbf{w}_c = [1 \ y]^T$ . By evaluating the output power  $J = \mathbf{w}_c^H \mathbf{S}_x \mathbf{w}_c$  and computing the Wirtinger derivative of  $J$  w.r.t.  $y^*$  [51], we find the constrained weights that give the least output power as

$$\mathbf{w}_c = [1 \ -\rho \sigma_v^2 / (\sigma_v^2 + \sigma_m^2)]^T. \quad (30)$$

It follows that the residual output noise power is given by

$$\mathbf{w}_c^H \mathbf{S}_n \mathbf{w}_c = \mathbf{w}_c^H (\mathbf{S}_m + \mathbf{S}_v) \mathbf{w}_c = \sigma_v^2 - \rho^2 \frac{\sigma_v^4}{\sigma_v^2 + \sigma_m^2}. \quad (31)$$

By dividing Eq. (31) by the input noise power  $\sigma_v^2$  we obtain the relative residual noise factor  $\eta$  (lower is better):

$$\eta = \frac{\mathbf{w}_c^H \mathbf{S}_n \mathbf{w}_c}{\sigma_v^2} = 1 - \rho^2 \frac{1}{1 + \sigma_m^2 / \sigma_v^2}. \quad (32)$$

The conventional MPDR cannot operate in single-channel settings and therefore acts as a bypass, yielding  $\eta = 1$ . With  $\text{SNR}_{\text{in}} = \sigma_s^2 / \sigma_v^2$  and the distortionless constraint preserving the target power  $\sigma_s^2$ , the output SNR becomes

$$\text{SNR}_{\text{out}}^{\text{cMPDR}} = \frac{\text{SNR}_{\text{in}}}{\eta}, \quad \text{SNR}_{\text{out}}^{\text{MPDR}} = \text{SNR}_{\text{in}}. \quad (33)$$

Thus, for  $\rho \neq 0$ ,  $\eta < 1$  and the cMPDR strictly increases the output SNR. It is also worth noting that, when  $\sigma_m^2 = 0$ , Eq. (31) matches the minimum achievable mean-squared error in estimating one complex RV from another when the two have correlation  $\rho$  (see [52], [53, Eq. 33]). The theoretical prediction in Eq. (32) is validated in Fig. 3, where the statistics used in the cMPDR are estimated from 200 realizations.

Equation (32) and Fig. 3 reveal the following properties. First, the relative residual noise factor of the cMPDR beamformer is strictly less than 1 when  $\rho \neq 0$ . As a result, the cMPDR improves the subband SNR, unlike the single- or multichannel Wiener filter, which does not affect it. Second, the amount of noise reduction increases with increasing correlation. Noise

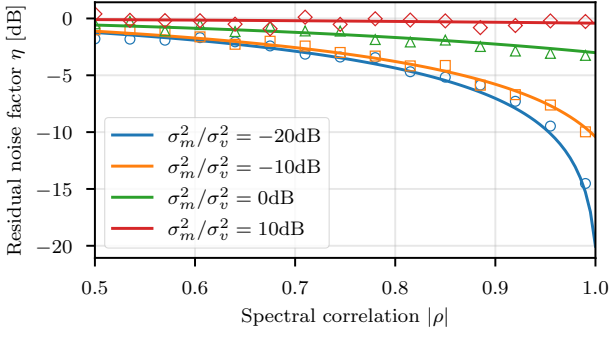


Fig. 3: Residual noise factor  $\eta$  [dB] versus spectral correlation  $|\rho|$  for different ratios  $\sigma_m^2/\sigma_v^2$ . Solid lines: Eq. (32). Markers: simulation measurements. For  $|\rho| < 0.5$ , all curves converge toward 0 dB.

reduction also increases as the power of the modulated target component  $\sigma_m^2$  decreases. In the limiting case of purely harmonic noise ( $|\rho| = 1$ ) and negligible modulated target interfering power ( $\sigma_m^2 \rightarrow 0$ ), the residual noise is exactly zero. Third, the cMPDR becomes less effective when the modulated target component has high power, which typically occurs at higher SNRs. For instance, if  $\sigma_m^2 = \sigma_s^2 = 100 \cdot \sigma_v^2$  (20 dB SNR), then  $\eta \approx 1 - \rho^2 \cdot 0.01 \approx 1$ , meaning the residual noise is approximately the same as for the conventional MPDR.

### C. Noise reduction performance: arbitrary $C_k$ and $M$

In the general case of arbitrary  $C_k$  and  $M$ , the following result holds.

**Theorem 1 (Monotonicity of output power).** *Consider the cMPDR beamformer for arbitrary  $C_k$  and  $M$  at frequency  $\omega_k$ , with positive definite covariance matrix  $\mathbf{S}_x$ . Let  $J^*(C_k)$  denote the minimum value of the optimization problem in Eq. (24) for a given  $C_k$ . Then  $J^*(C_k)$  is non-increasing with  $C_k$ .*

*Proof.* The cMPDR design in Eq. (24) is a strictly convex quadratic program with linear equality constraint, since  $\mathbf{S}_x$  is positive definite. Increasing  $C_k$  extends the observation vector  $\mathbf{x}$  with additional frequency-shifted components while preserving the same distortionless constraint. Hence, the feasible set for  $C_k + 1$  strictly contains the feasible set for  $C_k$ . Since the objective  $\mathbf{w}^H \mathbf{S}_x \mathbf{w}$  is strictly convex, the minimum over a larger feasible set cannot exceed the minimum over a subset.  $\square$

Since the distortionless constraint preserves the desired signal power, monotonic decrease of  $J^*(C_k)$  directly implies monotonic decrease of the residual noise power. Consequently, the output SNR of the cMPDR improves or remains unchanged as  $C_k$  increases. Experimental results confirm strict improvement whenever additional correlated components are included ( $\rho \neq 0$  and  $\sigma_v^2 > 0$  in Fig. 8b), in agreement with the literature [19].

## V. CONSTRUCTION OF THE MODULATION SETS $\mathcal{M}_k$

The multi-band signal  $\mathbf{x}(\mathcal{M}_k, \omega_k)$  serving as input to the cMPDR beamformer at frequency bin  $k$  is constructed by modulating the noisy input with the  $C_k$  frequencies in the modulation set  $\mathcal{M}_k$ , defined in Eq. (17). As discussed in Section IV-B, the output SNR per subband is maximized when the

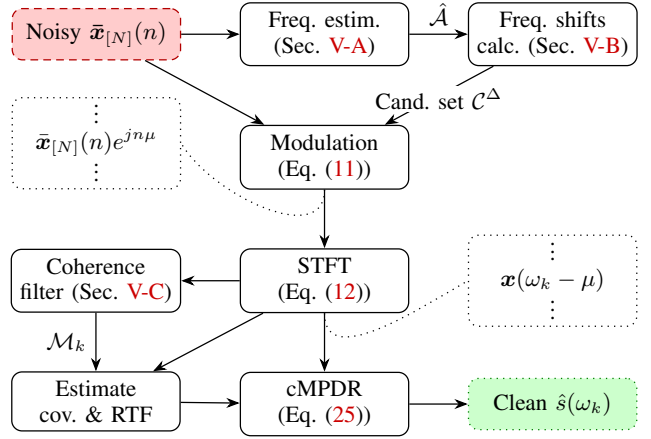


Fig. 4: Overview of the proposed method: harmonic frequency estimation, signal modulation, STFT, coherence filtering, and cMPDR beamforming.

modulation frequencies induce the strongest spectral correlation. In principle, this would require testing all possible frequencies and selecting those that maximize the correlation; however, such an exhaustive search is computationally infeasible. Instead, candidate frequency shifts are selected following established principles from the literature, which suggest including all combinations of cyclic frequencies of target and noise signals [19], [24]. To this end, we identify candidate shifts across all estimated resonant frequencies, accounting for potential estimation errors or missed components in the frequency-finding stage (Section V-A), and collect them in a candidate set. For each frequency bin  $k$ , the candidate modulations that yield the highest spectral coherence are then included in the modulation set  $\mathcal{M}_k$ .

Specifically, resonant noise frequencies are first estimated (Section V-A) and used to form the candidate set (Section V-B). The noisy signal is then modulated and transformed to the STFT domain, after which coherence filtering (Section V-C) identifies the most informative shifts. Based on these selected modulations, spectral-spatial covariance matrices and RTFs are estimated, and the beamforming weights are computed and applied to recover the denoised signal. The overall procedure is summarized in Fig. 4. Although resonant frequencies estimates are most accurate when obtained from noise-only recordings, satisfactory performance can still be achieved using the noisy mixture, especially in low-SNR scenarios.

### A. Estimation of cyclic or resonant frequencies

The resonant frequencies of the noise are estimated using the unmodified periodogram method [54, Ch. 4]. A rectangular window is preferred over smooth windows because, although smooth windows reduce variance, they broaden the main lobe and lower spectral resolution. Since CS-based methods are highly sensitive to frequency estimation errors [30], [29], maximizing spectral resolution is critical, motivating the choice of a single, long rectangular window over a Bartlett estimate with shorter windows and reduced variance. The periodogram

is computed as the magnitude-squared DFT of the noise-only signal at the reference microphone over  $N_v$  samples:

$$|\text{DFT}(\bar{v}_0(n))|^2, \quad n = 0, \dots, N_v - 1. \quad (34)$$

To improve frequency resolution, the DFT uses  $K_v > N_v$  points with zero-padding, yielding an interpolated periodogram. In practice,  $K_v$  should be chosen much larger than the STFT frame length  $K$  to ensure accurate estimation of the harmonic frequencies. Spectral peaks are located with `find_peaks` (SciPy 1.15.1), subject to constraints on minimum and maximum frequency, minimum peak distance, peak height ratio, and a maximum count. The top  $Q$  peaks in amplitude are selected as resonant frequency estimates and collected in a set  $\hat{A} = \{\hat{\alpha}_q\}_{q=1}^Q$ . Assuming the noise resonant frequencies remain constant, the periodogram estimation is performed only once per audio recording.

### B. Calculation of frequency shifts

Based on the estimated locations of the noise harmonics, we construct a set of candidate frequency shifts  $\mathcal{C}$  to be applied to the signal. Positive shifts move the signal content upwards in frequency. As alluded to in Fig. 2, the goal is to obtain frequency-shifted versions of the signal that are strongly correlated with the original, thereby enabling spectral beamforming. We consider two alternative constructions of  $\mathcal{C}$ :  $\mathcal{C}^\times$ , the integer-multiple set, which assumes a perfectly harmonic or CS model, and  $\mathcal{C}^\Delta$ , the difference-based set, which accommodates inharmonic or ACS processes. Their behavior is illustrated in Fig. 5, where the harmonics  $\{\alpha_1, \alpha_3, \alpha_4\}$  are shifted to align with the chosen working frequency  $\alpha_2$ .

1) *Integer-multiple shifts ( $\times$  strategy)*: In our previous work [30], the frequency shifts were computed based on the assumption that all harmonic components lie exactly at integer multiples of the estimated fundamental frequency  $\hat{\alpha}_1$ , yielding the following candidate modulation set:

$$\mathcal{C}^\times = \{-r\hat{\alpha}_1\}_{r=0}^{Q-1}. \quad (35)$$

While simple, this approach has two key limitations. First, real-world acoustic signals often deviate from the ideal harmonic model, as discussed in Section I, and such model mismatch degrades the performance of CS-based methods. Second, the method only considers negative frequency shifts, whereas including both negative and positive modulations is generally beneficial for performance.

2) *Difference-based shifts ( $\Delta$  strategy)*: To address the limitations of the integer-multiple approach, we propose a difference-based construction of the candidate set. The modulations are computed as all pairwise differences between the estimated resonant frequencies in  $\hat{A}$ , accounting for deviations from the ideal harmonic model:

$$\mathcal{C}^\Delta = \{\hat{\alpha}_q - \hat{\alpha}_r\}_{q,r=1}^Q \quad (36)$$

This strategy produces both positive and negative frequency shifts and remains effective even when the harmonics are arbitrarily far from the integer multiples of the fundamental frequency. Figure 5 compares the two modulation strategies for a working frequency  $\alpha_2$ . The first column shows the original

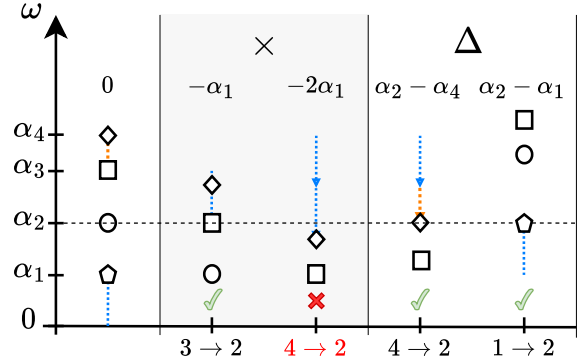


Fig. 5: Comparison of frequency-shift calculation strategies for aligning harmonics to working frequency  $\alpha_2$ . Column 1: original spectrum. Columns 2-3: integer-multiple downward shifts (Section V-B1); Columns 4-5: difference-based shifts (Section V-B2). Markers distinguish individual harmonics.

spectrum. Columns 2-3 apply the downward shifts from (35), which only align harmonics when they lie at exact integer multiples of  $\alpha_1$ . As seen with  $\alpha_4$  in column 3 in this example, any deviation from the ideal model causes the alignment to fail. In contrast, columns 4-5 use the difference-based shifts from (36), successfully aligning  $\alpha_4$  and  $\alpha_1$  to  $\alpha_2$ . This confirms that the difference-based approach yields correct alignment for arbitrary resonant frequencies.

Figure 7 shows SI-SDR results for the benchmark MPDR and the proposed cMPDR as a function of the noise inharmonicity. Higher inharmonicity means that the resonant frequencies deviate more from integer multiples of the fundamental. The cMPDR uses either the  $\times$  or  $\Delta$  strategy to compute frequency shifts, assuming the resonant frequencies are known in this toy example. Additional details are given in Section VI. When the noise is perfectly harmonic, both strategies perform equally well, and cMPDR achieves a 10 dB gain over the MPDR. As the inharmonicity increases, the  $\times$  strategy—based on integer-multiple assumptions—rapidly degrades, with no gains for as little as 0.5% inharmonicity, highlighting the sensitivity of strict harmonic models to deviations from perfect periodicity. In contrast, the  $\Delta$  strategy remains effective across all inharmonicity levels by aligning shifts with the observed spacing between resonant frequencies. The  $\Delta$  strategy is therefore adopted in all the experiments that follow.

### C. Coherence-based shift selection

Section V-B described two methods for identifying candidate modulations based on the estimated cyclic frequencies. This section introduces Algorithm 1 to select the optimal candidates for inclusion in the final modulation sets based on spectral coherence. Spectral coherence, defined in Eq. (8), quantifies the correlation between original and modulated signals at each frequency bin, and has been used to detect CS signals in noise [55], [56]. As demonstrated in Section IV-B, highly correlated components lead to improved noise suppression, making coherence an effective selection criterion.

The procedure is summarized in Algorithm 1, while the parameter values used in the implementation are listed in Table II. The selection process applies two sequential filtering

---

**Algorithm 1:** Coherence-based shift selection

---

**Input:** Candidate set  $\mathcal{C}^\Delta$ , noisy  $x(\omega_k)$ , coherence threshold  $\gamma_{\min}$ , max modulations  $C_{\max}$   
**Output:** Modulation sets  $\mathcal{M}_k$ ,  $k = 0, \dots, K - 1$   
**foreach**  $\mu \in \mathcal{C}^\Delta$  **do**  
    **for**  $k = 0$  **to**  $K - 1$   
        Compute coherence  $\hat{\gamma}_x(\mu, \omega_k)$  (Eq. (14))  
**for**  $k = 0$  **to**  $K - 1$   
     $\mathcal{M}_k \leftarrow \{\mu : \hat{\gamma}_x(\mu, \omega_k) \geq \gamma_{\min}\}$   
     $\mathcal{M}_k \leftarrow$  keep  $C_{\max}$  most coherent items in  $\mathcal{M}_k$

---

stages to reduce computational load. First, modulations must exceed a coherence threshold to qualify for inclusion. Second, when the number of qualifying modulations exceeds the user-specified maximum, the algorithm retains those with the highest coherence values.

## VI. EXPERIMENTAL SETUP

### A. Parameter estimation and algorithms

Computing the beamforming weights requires estimates of the noisy spectral-spatial covariance matrix, as well as the RTFs, all of which are unknown in practice. The matrix  $\hat{\mathbf{S}}_x$  is estimated from the noisy measurements using the ACP. Recursive averaging is applied to update  $\hat{\mathbf{S}}_x$  at each STFT frame. Diagonal loading is adopted to improve the conditioning of  $\hat{\mathbf{S}}_x$  and reduce the sensitivity of the beamformer to errors in the estimated RTF vector  $\mathbf{a}$  [57]. Specifically, a scaled identity matrix is added to the noisy covariance matrix, with the scaling chosen to bound the condition number of the loaded matrix [58]. The RTFs  $\mathbf{a}(\omega_k)$  are estimated using the covariance whitening (CW) technique [59]. The noise covariance matrix  $\hat{\mathbf{S}}_v$ , required to perform CW, is estimated from a separate noise-only segment. The conventional MPDR beamformer is used as a benchmark; its spatial covariance matrices are estimated via standard recursive averaging with diagonal loading, and its RTFs are obtained using the same CW procedure as for the proposed method. To assess the impact of RTF estimation on performance, we also evaluate oracle versions of the beamformers, denoted as MPDR+ and cMPDR+, that assume access to the true RTFs.

Frequency estimation (Section V-A) is performed on the same noise-only realization used to estimate the covariance matrices. For peak selection after frequency estimation with the periodogram, we enforce a minimum separation between peaks and limit both the peak amplitude ratio and the maximum number of detected peaks. The admissible frequency range is set to 20 Hz to 2.5 kHz, as preliminary experiments showed that higher resonant frequencies are difficult to estimate with sufficient accuracy. Coherence filtering (Section V-C) is based on the noisy data. Estimation and algorithmic parameters are reported in Table II.

TABLE II: Estimation and algorithmic parameters.

Parameter	Value
DFT size (STFT)	$K = 2048$
STFT window	Square-root Hann
STFT overlap	75%
Covariance smoothing constant	$\beta_x = 0.95$
Max condition number	$\kappa_0 = 1000$
Minimum peak distance	20 Hz
Maximum peak ratio	$10^4$
Maximum number of peaks	$Q = 20$
Periodogram DFT size	$K_v = 2^{17}$
Admissible frequency range	20 Hz – 2.5 kHz
PSD dynamic range	$D_{\text{PSD}} = 1000$
Coherence threshold	$\gamma_{\min} = 0.6$
Maximum retained shifts	$C_{\max} = 8$

TABLE III: Simulation and data generation parameters.

Parameter	Value
Sampling frequency	$f_s = 16$ kHz
Number of microphones	$M = 2$
Inter-microphone spacing	8 cm
Noisy sequence duration	2 s
Noise-only sequence duration	2 s
Interferer SNR	-10 dB
Self-noise SNR	30 dB
RIR dataset	Bar-Ilan
Monte Carlo runs	50

### B. Simulation parameters and metrics

Performance is evaluated using SI-SDR for both simulated and real data [60]. For real recordings, we additionally report short-time objective intelligibility (STOI) scores [61]. All results are shown as score improvements, computed by subtracting the score of the unprocessed signal at the first microphone from the score of each beamformer.

We simulate a target speech source and an interfering noise source, both modeled as omni-directional point sources. Spatially uncorrelated white Gaussian noise is added to simulate microphone self-noise. Speech signals are recordings of the Harvard sentences, uttered by either a male or a female speaker [62]. The room impulse responses (RIRs) for the target and interferer are randomly selected from the Bar-Ilan dataset [63]. For synthetic noise experiments, we select from 26 RIRs with  $\text{RT60} = 0.61$  s, while for real noise experiments we use 26 RIRs with  $\text{RT60} = 0.16$  s, unless otherwise stated. The angles and the distances between the point sources and the array vary independently at each Monte Carlo trial. Results are averaged over multiple Monte Carlo runs, each using different RIRs, noise realizations, and target signals. For each run, a speech segment and a noise segment are randomly selected and weighted to obtain the desired SNR, which is defined with respect to the target and noise powers at the reference microphone, and then summed to form a mixture of the desired length. Lines in the plots indicate mean values, and shaded areas correspond to 95% confidence intervals. The default simulation parameters are summarized in Table III.

### C. Noise datasets

The cMPDR is evaluated against three different noise types: synthetic, CS noise; real, ACS motor noise; real, mostly non-stationary environmental noise.

1) *Synthetic harmonic noise*: The synthetic CS noise is modeled as a random harmonic signal with adjustable correlation across harmonic components. The model allows controlled variation of the correlation level, reflecting the partial correlation typically observed in real noise. Formally, let  $\{\bar{u}(n), n \in \mathbb{Z}\}$  be a CS process where a scalar parameter  $\beta$  controls whether all harmonics share the same amplitude variation over time or vary independently:

$$\bar{u}(n) = \sum_{p=1}^{P_u} \bar{a}_p(n; \beta) \cos(\omega_p n + \phi_p), \quad (37a)$$

$$\bar{a}_p(n; \beta) = [\beta \bar{b}(n) + (1 - \beta) \bar{c}_p(n)] d_p, \quad (37b)$$

where  $\omega_p = \omega_0 p$ . The frequency  $\omega_0$  is a RV drawn from  $2\pi \cdot \mathcal{U}(60, 150)$ , and the phases  $\phi_p$  are independently drawn from  $\mathcal{U}(-\pi, \pi)$ . The processes  $\{\bar{b}(n)\}$  and  $\{\bar{c}_p(n)\}$  are WSS and describe the temporal amplitude fluctuations. The amplitudes  $d_p$  are independent RVs drawn from  $\mathcal{U}(1, 10)$ . Both  $\{\bar{b}(n)\}$  and  $\{\bar{c}_p(n)\}$  consist of independent Gaussian RVs distributed as  $\mathcal{N}(0, 10)$  and lowpass filtered by a 4th order Butterworth filter with cutoff frequency  $f_c = 5$  Hz. The parameter  $\beta \in [0, 1]$  controls the correlation of the amplitude envelopes across components, where  $\beta$  closer to 1 gives more spectral correlation. The spectral correlation is set to  $\beta = 0.8$  unless specified differently. The number of components is set to  $P_u = 16$ .

2) *Real UAV motor noise (DREGON dataset)*: The second noise set is a subset of the DREGON dataset [64] that consists of 21 motor-only recordings from a quadrotor unmanned aerial vehicle (UAV, commonly known as drone) equipped with an 8-channel cube-shaped microphone array. The UAV was suspended on a nylon string and held stationary to capture pure motor noise under low-reverberation conditions. The recordings include individual propeller noise at different rotational speeds, as well as combined engine noise. The initial and final 10 s of each recording are trimmed to remove quiet segments and transients from motor start-up and shutdown. This noise set exhibits pseudo-harmonic, ACS noise, with spectral peaks at approximate multiples of the motor rotation frequency, making it the primary real-world benchmark for cMPDR.

3) *Real non-stationary noise (MUSAN dataset)*: The third noise set consists of recordings drawn from the Freesound portion of the MUSAN corpus [65], as adapted by Ko *et al.* [66]. We used the public OpenSLR release of this dataset [67]. It comprises a wide range of 843 mostly non-stationary noise signals that are not aligned with the assumptions underlying cMPDR. This dataset is used to evaluate behavior outside the targeted ACS setting. In these conditions, the cyclic advantage is expected to vanish, such that the cMPDR effectively reduces to MPDR and does not incur additional performance loss.

## VII. EXPERIMENTAL RESULTS

Figure 6 provides a qualitative example of the noise suppression achieved by the proposed method. In the presence of strong

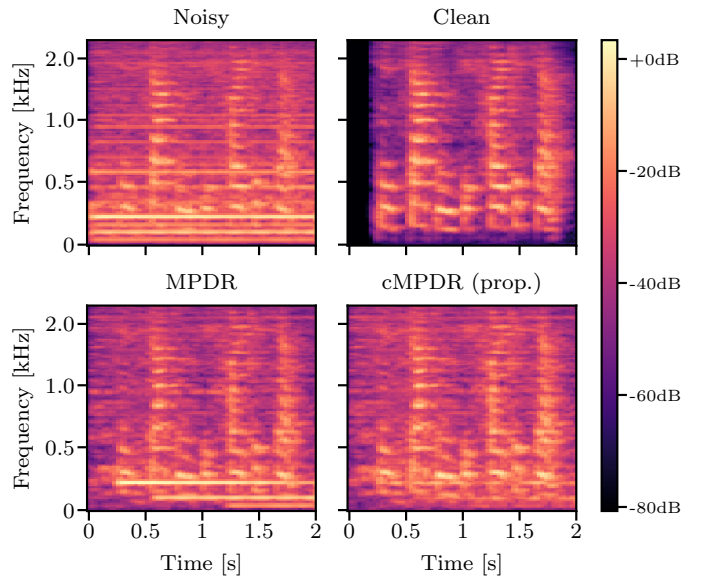


Fig. 6: Mel spectrograms of noise-free-sound-0002 from the MUSAN corpus, showing noisy input ( $-5$  dB SNR), clean target, and outputs of the MPDR and proposed cMPDR. Cyclostationarity-aware processing allows the cMPDR to suppress strong tonal noise.

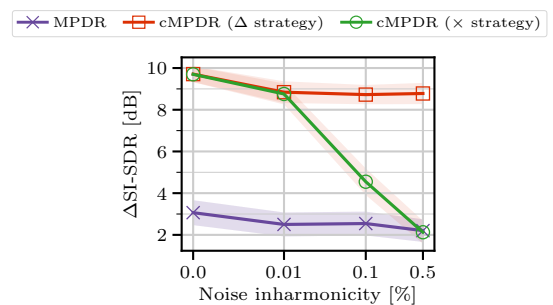


Fig. 7: Comparison of the  $\times$  and the  $\Delta$  strategies for calculating frequency shifts using synthetic harmonic noise. Default parameters are given in Section VI-C1 and Table III; here, resonant frequencies are assumed known and only inharmonicity is varied.

tonal components, the cMPDR can better attenuate structured interference than the MPDR, resulting in clearer speech. The following subsections provide systematic quantitative evaluations across three noise datasets.

### A. Synthetic harmonic noise experiments

This section compares the performance of the MPDR and cMPDR beamformers on the synthetic noise set, which features random harmonic signals with adjustable spectral correlation (Section VI-C1).

Figure 7, already discussed in Section V-B, compares the  $\times$  and the  $\Delta$  strategies for computing frequency shifts under varying noise inharmonicity, assuming known resonant frequencies. These are defined as  $\hat{\omega}_p = \omega_0 p(1 + \omega_{\text{err}}/100)$ . The performance of the  $\Delta$  strategy remains stable across all tested inharmonicity levels and is therefore used in all subsequent experiments.

Figure 8 reports the output SI-SDR on speech corrupted by synthetic noise. In Figs. 8a to 8d, resonant frequencies

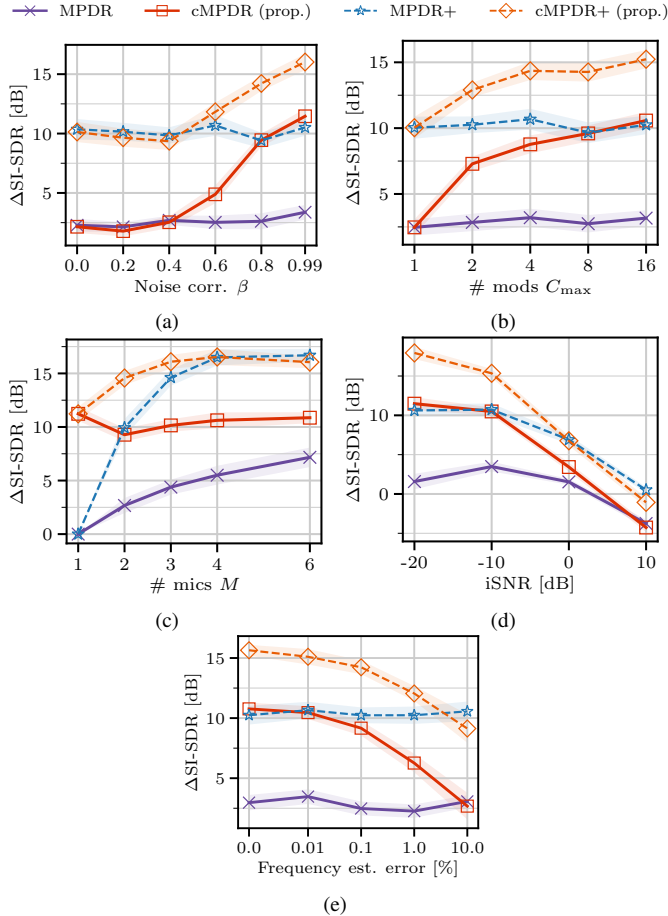


Fig. 8: Synthetic harmonic noise experiments. SI-SDR improvements as a function of spectral correlation, maximum number of modulations, number of microphones, interferer SNR, and frequency estimation error. Unless otherwise specified, parameters are set to the default values in Table III. Oracle variants (“+”) use the true RTF.

are estimated via the periodogram. Figure 8a shows that the performance of the proposed cMPDR improves with increasing noise correlation  $\beta$ . For  $\beta > 0.8$ , it even outperforms the oracle MPDR, in agreement with the theoretical result in Section IV-B, which favors cMPDR for highly correlated noise. Figure 8b shows the effect of  $C_{\max}$ , the maximum number of modulations per set. With  $C_{\max} = 2$ , the cMPDR already achieves a 5 dB gain over the MPDR. Increasing  $C_{\max}$  further improves SI-SDR, providing empirical support for Theorem 1. Figure 8c shows that increasing the number of microphones boosts performance for all methods except the cMPDR. This occurs because the high spectral correlation ( $\beta = 0.8$ ) makes spectral cues dominate over spatial cues. While cMPDR does benefit from more microphones in real-data experiments (Figs. 9b and 9f) and in additional synthetic experiments with  $\beta = 0.65$  (not shown), it already performs well even with a single microphone. Finally, Fig. 8d presents SI-SDR as a function of interferer SNR (iSNR). In the low-SNR regime, both the proposed and oracle cMPDR outperform the oracle MPDR, confirming their robustness. At iSNRs above 10 dB, the cyclic methods perform similarly to the benchmark, consistent with Eq. (32).

Figure 8e evaluates the sensitivity of the proposed beam-

former to errors in the estimated resonant frequencies. Unlike Fig. 7, which assumes access to true but increasingly inharmonic frequencies, here the true resonant frequencies are perturbed before computing the candidate shifts using  $\tilde{\omega}_p = \omega_0 p(1 + \omega_{\text{err}}/100 \cdot \mathcal{U}(-1, 1))$ . MPDR and MPDR+ do not use frequency information and are therefore not affected. On the other hand, cMPDR outperforms MPDR in SI-SDR by 8 dB with perfect estimation and by 4 dB with 1% error, while converging to MPDR performance at 10% error.

### B. Real UAV motor noise experiments (DREGON dataset)

This section analyzes performance in recovering target speech buried in noise from UAV motor recordings. Each row of Fig. 9 corresponds to a different evaluation metric, and each column to a different parameter. In terms of SI-SDR, increasing the number of modulating frequencies generally improves performance, with gains up to 5.2 dB for  $C_{\max} = 16$  (Fig. 9a). More microphones are also beneficial, though gains are smaller for methods relying on CW to estimate RTFs compared to the “+” variants that use oracle RTFs (Fig. 9b). As in the synthetic experiments, the cMPDR shows clear advantages in the low-SNR regime, while matching the MPDR performance for iSNRs  $\geq 0$  (Fig. 9c). Performance under increasing reverberation time (RT60) is shown in Fig. 9d, with all methods degrading with higher RT60. STOI trends follow those of SI-SDR closely, with cMPDR achieving up to 0.06 improvement over the MPDR (Figs. 9e to 9h). Interestingly, increasing  $C_{\max}$  beyond 4 does not lead to consistent improvements in either SI-SDR or STOI, suggesting that most of the benefit from additional cyclic components is captured at relatively low values.

### C. Real non-stationary noise experiments (MUSAN dataset)

Figure 10 reports SI-SDR and STOI improvements under non-stationary environmental noise from the MUSAN dataset, as a function of the number of microphones  $M$  and interferer SNR. In contrast to the ACS scenarios in Sections VII-A and VII-B, MPDR and cMPDR exhibit nearly identical performance across all tested conditions. The oracle variants MPDR+ and cMPDR+ also approximately coincide for both SI-SDR and STOI. Cyclic processing does not offer consistent benefits in this setting. In most MUSAN recordings, the absence of persistent spectral correlation keeps the coherence of candidate shifts below  $\gamma_{\min}$ , leading to their exclusion from the modulation sets. As a result, the spatial-spectral covariance matrix estimate reduces to the conventional spatial covariance matrix, and cMPDR reduces to MPDR. These results confirm that the proposed method does not suffer performance losses when the noise deviates from the ACS model. When cyclic structure is absent, the coherence-based selection mechanism effectively reverts the algorithm to standard MPDR behavior, preserving baseline performance under general non-stationary interference.

### D. Discussion

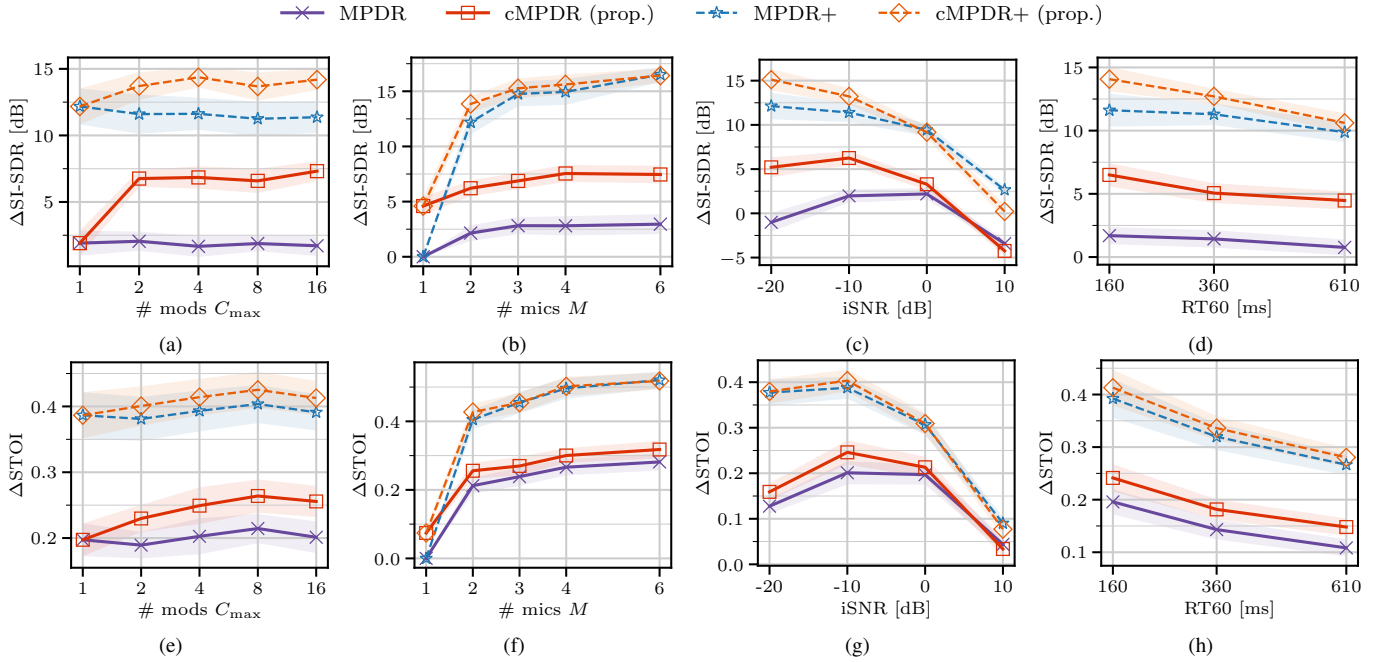


Fig. 9: Real UAV motor noise experiments (DREGON dataset). Improvements in terms of SI-SDR and STOI as a function of maximum number of modulations, number of microphones, interferer SNR and RT60. Unless otherwise specified, parameters are set to the default values in Table III. Oracle variants (“+”) use the true RTF.

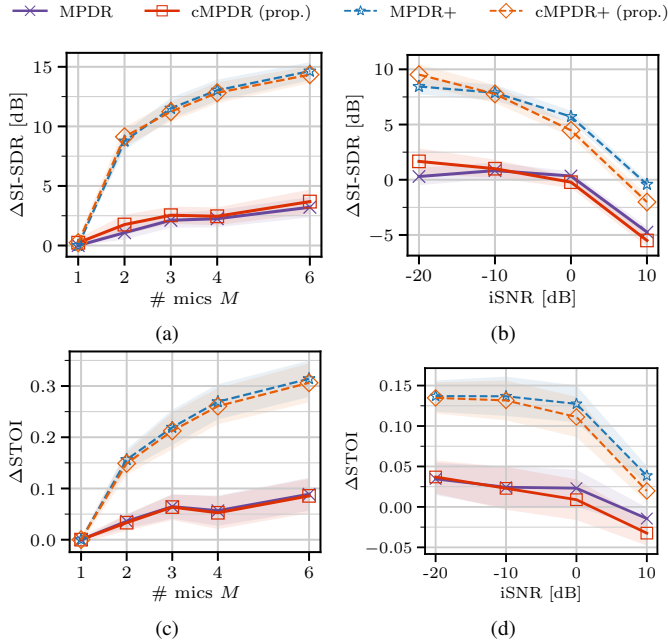


Fig. 10: Real non-stationary noise experiments (MUSAN dataset). SI-SDR improvements as a function of number of microphones and interferer SNR. Unless otherwise specified, parameters are set to the default values in Table III. Oracle variants (“+”) use the true RTF.

1) *Computational complexity*: Computing the cMPDR weights requires inversion of the spectral-spatial covariance matrix of dimension  $MC_k$  at each frequency bin and time frame (Eq. (25)). In the worst case, direct inversion has cubic complexity  $O((MC_k)^3)$ . Since  $C_k$  may reach  $C_{\max}$ , this represents a potential increase in computational cost compared

to the conventional MPDR beamformer.

However, this bound corresponds to a pessimistic worst-case scenario. First, the covariance matrix is estimated via recursive averaging, where each new observation contributes a rank-1 update. Accordingly, the inverse can be updated efficiently using the Sherman-Morrison lemma, reducing the per-frame complexity by approximately one order of magnitude. Second, the dimensionality increase occurs only in bins exhibiting high spectral coherence. For non-harmonic bins,  $C_k = 1$ , and the cMPDR reduces exactly to the MPDR with identical complexity. Empirically, bins for which  $C_k > 1$  constitute a small fraction of the spectrum (approximately 2% in the DREGON dataset, i.e., about 20 out of  $K/2 + 1 = 1025$  bins). Thus, additional computation is concentrated on spectrally coherent components while standard complexity is retained elsewhere, yielding a favorable performance-complexity trade-off in practice. Increasing  $C_k$ , however, also enlarges the covariance matrix to be estimated, which becomes a concern in dynamic environments, as discussed next.

2) *Behavior in non-stationary noise*: The proposed cMPDR does not fail in non-stationary noise conditions. The coherence-based shift selection discards frequency shifts that give weak spectral coherence, and the method reduces to conventional MPDR. Matrix conditioning is stabilized by diagonal loading (Section VI) and no instability is observed in the evaluated scenarios.

However, the current implementation is not adaptive to varying harmonic structures, and is most effective when the interferer exhibits a stable spectral profile (e.g. a motor at approximately constant speed). Tracking time-varying harmonic patterns is fundamentally more challenging than tracking narrowband spatial covariance matrices. Whereas spatial co-

variance matrices scale approximately by a scalar factor when sources are stationary, spectral covariance matrices are tied to the instantaneous periodicities of the signal and change with every shift in operating regime (e.g. motor speed or load). Developing adaptive extensions for such scenarios remains an important direction for future work.

## VIII. CONCLUSIONS

This work proposed the cMPDR beamformer, extending the MPDR framework by exploiting both spatial and spectral correlations of almost-cyclostationary interference. Two mechanisms enable this: a difference-based shift calculation that derives modulation frequencies from pairwise differences between estimated resonant frequencies, avoiding assumptions of a rigid harmonic grid; and a coherence-based shift selection that removes weakly correlated spectral components, allowing the method to reduce to conventional MPDR when spectral redundancy is absent.

Theoretical analysis established that residual noise power decreases monotonically with the number of coherent cyclic components, and that the performance advantage over spatial-only beamforming is directly proportional to the degree of spectral correlation. Experiments on synthetic harmonic noise, real UAV motor recordings, and non-stationary noise confirmed these predictions: the cMPDR achieves consistent SI-SDR and STOI improvements over the MPDR benchmark, with gains of up to 5 dB in low-SNR conditions, while matching MPDR performance when the noise lacks persistent spectral structure. The method is most effective for interferers with stable spectral properties. Extending the framework to track time-varying harmonic structures remains an important direction for future work.

## REFERENCES

- [1] S. S. M. Zaki, A. Razali, and M. M. A. Qahar, "Method for Measuring Speech Enhancement of Electronic Hearing Protection Device: A Systematic Review," *IJUM Medical Journal Malaysia*, 2025.
- [2] Y. Luo, C. Han, N. Mesgarani, E. Ceolini, and S.-C. Liu, "FaSNNet: Low-Latency Adaptive Beamforming for Multi-Microphone Audio Processing," in *2019 IEEE Automatic Speech Recognition and Understanding Workshop (ASRU)*, 2019.
- [3] K. Tesch and T. Gerkmann, "Insights Into Deep Non-linear Filters for Improved Multi-channel Speech Enhancement," *IEEE/ACM Trans. Audio Speech Lang. Process.*, 2023.
- [4] C. Quan and X. Li, "SpatialNet: Extensively Learning Spatial Information for Multichannel Joint Speech Separation, Denoising and Dereverberation," *IEEE/ACM Transactions on Audio, Speech, and Language Processing*, 2024.
- [5] S. S. Shetu, S. Chakrabarty, O. Thiergart, and E. Mabande, "Ultra Low Complexity Deep Learning Based Noise Suppression," in *Proc. ICASSP*, 2024.
- [6] X. Hao, X. Su, Z. Wang, H. Zhang, and Batushiren, "UNetGAN: a robust speech enhancement approach in time domain for extremely low signal-to-noise ratio condition," in *Proc. INTERSPEECH*, 2019.
- [7] K. M. B. Schulz, H. Wittmann, L. Hackenberg, T. Jürgens, and J. Tchorz, "Effects of low-latency deep-learning-based noise reduction on speech intelligibility for normal hearing, hearing-impaired listeners and cochlear implant users," *Frontiers in Audiology and Otology*, 2026.
- [8] A. Cohen, D. Wong, J.-S. Lee, and S. Gannot, "Explainable DNN-Based Beamformer With Postfilter," *IEEE Transactions on Audio, Speech and Language Processing*, 2025.
- [9] J. Capon, "High-resolution frequency-wavenumber spectrum analysis," *Proceedings of the IEEE*, 1969.
- [10] S. Gannot, E. Vincent, S. Markovich-Golan, and A. Ozerov, "A Consolidated Perspective on Multimicrophone Speech Enhancement and Source Separation," *IEEE/ACM Transactions on Audio, Speech, and Language Processing*, 2017.
- [11] S. Doclo, S. Gannot, M. Moonen, and A. Spriet, "Acoustic Beamforming for Hearing Aid Applications," in *Handbook on Array Processing and Sensor Networks*. John Wiley & Sons, Ltd, 2010.
- [12] S. Gannot, D. Burshtein, and E. Weinstein, "Signal enhancement using beamforming and nonstationarity with applications to speech," *IEEE Transactions on Signal Processing*, 2001.
- [13] A. Napolitano, "A - Nonstationary signal analysis," in *Cyclostationary Processes and Time Series*. Academic Press, 2020.
- [14] W. A. Gardner, *Statistical Spectral Analysis: A Nonprobabilistic Theory*. Prentice-Hall, Inc., 1986.
- [15] —, *Cyclostationarity in Communications and Signal Processing*. IEEE Press, 1994.
- [16] B. Feher, "Short Overview of Cyclostationary Signal Processing," Technische Univ. Delft (Netherlands). Dept. of Applied Physics., Tech. Rep., 1995.
- [17] W. A. Gardner, A. Napolitano, and L. Paura, "Cyclostationarity: Half a century of research," *Signal Processing*, 2006.
- [18] J. Antoni, "Cyclostationarity by examples," *Mechanical Systems and Signal Processing*, 2009.
- [19] W. Gardner, "Cyclic Wiener filtering: Theory and method," *IEEE Trans. Commun.*, Jan./1993.
- [20] S. Schell and W. Gardner, "Progress on signal-selective direction finding," in *Fifth ASSP Workshop on Spectrum Estimation and Modeling*, 1990.
- [21] P. Chevalier and A. Maurice, "Constrained beamforming for cyclostationary signals," in *Proc. ICASSP*, 1997.
- [22] —, "Blind and informed cyclic array processing for cyclostationary signals," in *9th European Signal Processing Conference (EUSIPCO 1998)*, 1998.
- [23] J. Zhang, "Blind adaptive cyclic filtering and beamforming algorithms," Ph.D. dissertation, McMaster University, Hamilton, Ontario, 2001. [Online]. Available: <http://hdl.handle.net/11375/7218>
- [24] H. Zhang, A. Abdi, and A. Haimovich, "Reduced-Rank Multi-Antenna Cyclic Wiener Filtering for Interference Cancellation," in *MILCOM 2006 - 2006 IEEE Military Communications Conference*, 2006.
- [25] K.-L. Du and M. N. S. Swamy, "A Class of Adaptive Cyclostationary Beamforming Algorithms," *Circuits, Systems & Signal Processing*, 2008.
- [26] C. Zhang, R. Wang, L. Yu, Y. Xiao, Q. Guo, and H. Ji, "Localization of cyclostationary acoustic sources via cyclostationary beamforming and its high spatial resolution implementation," *Mechanical Systems and Signal Processing*, 2023.
- [27] H. Fletcher, "Normal Vibration Frequencies of a Stiff Piano String," *The Journal of the Acoustical Society of America*, 1964.
- [28] University of Iowa Electronic Music Studios, "Musical instrument samples," 2011, [Online]. Available at <https://theremin.music.uiowa.edu/MIS.html>.
- [29] O. A. Y. Ojeda and J. Grajal, "Adaptive-FRESH Filters for Compensation of Cycle-Frequency Errors," *IEEE Transactions on Signal Processing*, 2010.
- [30] G. Bologni, R. Heusdens, and R. C. Hendriks, "Cyclic Multichannel Wiener Filter for Acoustic Beamforming," in *2025 IEEE Workshop on Applications of Signal Processing to Audio and Acoustics (WASPAA)*, 2025.
- [31] J. R. Jensen, S. Karimian-Azari, M. G. Christensen, and J. Benesty, "Harmonic beamformers for speech enhancement and dereverberation in the time domain," *Speech Communication*, 2020.
- [32] J. Zhang, K. Wong, Z. Luo, and P. Ching, "Blind adaptive FRESH filtering for signal extraction," *IEEE Transactions on Signal Processing*, 1999.
- [33] R. G. Gallager, "Principles of Digital Communication," 2007.
- [34] W. Gardner, "Exploitation of spectral redundancy in cyclostationary signals," *IEEE Signal Process. Mag.*, 1991.
- [35] J. Antoni and D. Hanson, "Detection of Surface Ships From Interception of Cyclostationary Signature With the Cyclic Modulation Coherence," *IEEE Journal of Oceanic Engineering*, 2012.
- [36] G. Giannakis, *Cyclostationary Signal Analysis*. CRC Press, 2009, pp. 1–32.
- [37] W. Gardner, "Measurement of spectral correlation," *IEEE Transactions on Acoustics, Speech, and Signal Processing*, 1986.
- [38] J. Antoni, "Cyclic spectral analysis of rolling-element bearing signals: Facts and fictions," *Journal of Sound and Vibration*, 2007.
- [39] R. Roberts, W. Brown, and H. Loomis, "Computationally efficient algorithms for cyclic spectral analysis," *IEEE Signal Processing Magazine*, 1991.

- [40] P. Borghesani and J. Antoni, "A faster algorithm for the calculation of the fast spectral correlation," *Mechanical Systems and Signal Processing*, 2018.
- [41] J. K. Alsalaet, "Fast Averaged Cyclic Periodogram method to compute spectral correlation and coherence," *ISA Transactions*, 2022.
- [42] A. Gilloire and M. Vetterli, "Adaptive filtering in subbands with critical sampling: analysis, experiments, and application to acoustic echo cancellation," *IEEE Transactions on Signal Processing*, 1992.
- [43] Y. Avargel and I. Cohen, "System Identification in the Short-Time Fourier Transform Domain With Crossband Filtering," *IEEE Transactions on Audio, Speech, and Language Processing*, 2007.
- [44] X. Li, L. Girin, S. Gannot, and R. Horaud, "Multichannel Speech Separation and Enhancement Using the Convolutional Transfer Function," *IEEE/ACM Transactions on Audio, Speech, and Language Processing*, 2019.
- [45] J. Chen and J. Benesty, "Single-channel noise reduction in the STFT domain based on the bifrequency spectrum," in *Proc. ICASSP*, 2012.
- [46] H. Huang, L. Zhao, J. Chen, and J. Benesty, "A minimum variance distortionless response filter based on the bifrequency spectrum for single-channel noise reduction," *Digital Signal Processing*, 2014.
- [47] R. Talmon, I. Cohen, and S. Gannot, "Relative Transfer Function Identification Using Convolutional Transfer Function Approximation," *IEEE Transactions on Audio, Speech, and Language Processing*, 2009.
- [48] J. F. Adlard, "Frequency Shift Filtering for Cyclostationary Signals," Ph.D. dissertation, University of York, 2000, unpublished. [Online]. Available: <https://theses.whiterose.ac.uk/id/eprint/14178/>
- [49] B. Picinbono, "On circularity," *IEEE Transactions on Signal Processing*, 1994.
- [50] J. Benesty, J. Chen, and Y. Huang, "Study of the widely linear Wiener filter for noise reduction," in *Proc. ICASSP*, 2010.
- [51] D. H. Brandwood, "A complex gradient operator and its application in adaptive array theory," *IEE Proceedings F (Communications, Radar and Signal Processing)*, 1983.
- [52] H. Kasasbeh, R. Viswanathan, and L. Cao, "Noise Correlation Effect on Detection: Signals in Equicorrelated or Autoregressive(1) Gaussian," *IEEE Signal Process Lett*, 2017.
- [53] T. Adali and P. J. Schreier, "Optimization and Estimation of Complex-Valued Signals: Theory and applications in filtering and blind source separation," *IEEE Signal Processing Magazine*, 2014.
- [54] P. G. Stoica, R. Moses, P. Stoica, and R. L. Moses, *Spectral Analysis of Signals*. Pearson, Prentice Hall, 2005.
- [55] K. Kim, I. A. Akbar, K. K. Bae, J.-S. Um, C. M. Spooner, and J. H. Reed, "Cyclostationary Approaches to Signal Detection and Classification in Cognitive Radio," in *2007 2nd IEEE International Symposium on New Frontiers in Dynamic Spectrum Access Networks*. IEEE, 2007.
- [56] J. X. Yang, "Cyclostationary beamforming for multiple cycle frequencies estimation and detection," Ph.D. dissertation, Nanyang Technological University, 2019.
- [57] H. Cox, R. Zeskind, and M. Owen, "Robust adaptive beamforming," *IEEE Transactions on Acoustics, Speech, and Signal Processing*, 1987.
- [58] A. H. Moore, S. Hafezi, R. R. Vos, P. A. Naylor, and M. Brookes, "A Compact Noise Covariance Matrix Model for MVDR Beamforming," *IEEE/ACM Transactions on Audio, Speech, and Language Processing*, 2022.
- [59] S. Markovich-Golan and S. Gannot, "Performance analysis of the covariance subtraction method for relative transfer function estimation and comparison to the covariance whitening method," in *Proc. ICASSP*, 2015.
- [60] J. L. Roux, S. Wisdom, H. Erdogan, and J. R. Hershey, "SDR – Half-baked or Well Done?" in *Proc. ICASSP*, 2019.
- [61] C. H. Taal, R. C. Hendriks, R. Heusdens, and J. Jensen, "An Algorithm for Intelligibility Prediction of Time-Frequency Weighted Noisy Speech," *IEEE Transactions on Audio, Speech, and Language Processing*, 2011.
- [62] "IEEE recommended practice for speech quality measurements," pp. 225–246, 1969.
- [63] E. Hadad, F. Heese, P. Vary, and S. Gannot, "Multichannel audio database in various acoustic environments," in *2014 14th International Workshop on Acoustic Signal Enhancement (IWAENC)*, 2014.
- [64] M. Strauss, P. Mordel, V. Miguet, and A. Deleforge, "DREGON: Dataset and Methods for UAV-Embedded Sound Source Localization," in *Proc. IROS*, 2018.
- [65] D. Snyder, G. Chen, and D. Povey, "MUSAN: A Music, Speech, and Noise Corpus," 2015.
- [66] T. Ko, V. Peddinti, D. Povey, M. L. Seltzer, and S. Khudanpur, "A study on data augmentation of reverberant speech for robust speech recognition," in *Proc. ICASSP*, 2017.
- [67] —, "Room impulse response and noise database," <https://www.openslr.org/28/>.